Shape-shifting panel from 3D printed undulated ribbon lattice

Filippo Agnelli, Michele Tricarico, Andrei Constantinescu

Shape-shifting panel from 3D printed undulated ribbon lattice

Filippo Agnelli[a], Michele Tricarico[b], Andrei Constantinescu[a,*]

[a] *Laboratoire de Mécanique des Solides, CNRS, École polytechnique, Institut polytechnique de Paris, 91128 Palaiseau, France*
[b] *MMC Laboratory, Department of Engineering Science, University of Oxford, Parks Road, Oxford, OX1 3PJ, United Kingdom*

Abstract

Materials that change their shape in response to external stimuli open up new prospects for efficient and versatile design and shaping of three-dimensional objects. Here, we present a novel class of micro-structures exhibiting an extension-bending coupling (EBC) effect, that can be harnessed as an elementary building block for shape-shifting panels. They are built with a single material as a network of undulated ribbons. The deformations mechanisms of both single and connected undulated ribbons are analysed using the finite element method to explain the main features of the EBC mechanism. For a particular micro-structure of the proposed class, the elastic response is investigated both under small strain assumption combining two-scale homogenization with Kirchhoff-Love plate theory, and at finite strains relying on numerical analysis. The range of achievable EBC ratio is then assessed with respect to the geometric parameters of the unit cell. Patterned specimens are manufactured using a commercial FFF Ultimaker 3D printer and are mechanically tested at finite strain up to 20%. The displacement measured by point tracking match the predictions from the finite element simulations and indicate that the structure maintain its properties at finite strain. Moreover, a tensile test load with point-like boundary is proposed to highlight exceptional out of plane displacement. The proposed ribbon based architectures can be combined with active materials for the actuation of shape shifting structures, like soft robots, control systems and power devices.

Keywords: 3D printing, metamaterial, shape shifting, panels, undulated ribbons.

1. Introduction

The morphing of shell-based structures into programmable three-dimensional geometries is a ubiquitous mechanism found in nature, which is attracting increasing interest for technological applications [1]. In engineering, flat panels are traditionally enticing due to their high strength-to-weight ratio which makes them structurally efficient. Including programmability into such structures expands the potential of available manufacturing techniques and increases the fabrication throughput for three-dimensional objects of complex geometries [2–4]. In addition, it unleashes new functionalities suitable for exploring harsh or inaccessible environments [5, 6] and delivering increasingly large and complex payloads [7, 8]. Several concepts have already been reported for a broad range of length scales, from minimally invasive surgery [9, 10], to automotive [11], aeronautics [12] and up to space sector [13–15].

Systems with shape-shifting capacities are obtained through "transformation mechanisms", tailored by the micro-architecture of the material. Recent advances in digital manufacturing technologies such as 3D printing [16–18] and laser cutting [19–21] have opened the way to a wide range of novel micro-architectures that couple locally prescribed in-plane kinematics to changes in curvature. These micro-architectures can be regrouped into model classes: origami structures, which feature axially-rigid but potentially-flexible panels connected by foldable creases, may be turned into nearly arbitrary shapes [22–24]. Yet, due to the independent folding motions of individual folds, they are challenging to fold [25, 26] or actuate. Kirigami tessellations, *i.e.* cut-patterned panel, allow compact flat shapes to conform approximately to any prescribed target shape in two or three dimensions [27–29]. Folding and cut patterns may be combined to design shape-shifting concepts as demonstrated in [30]. Compliant mechanism-like structures, featuring

*Corresponding author
Email address: andrei.constantinescu@polytechnique.edu (Andrei Constantinescu)

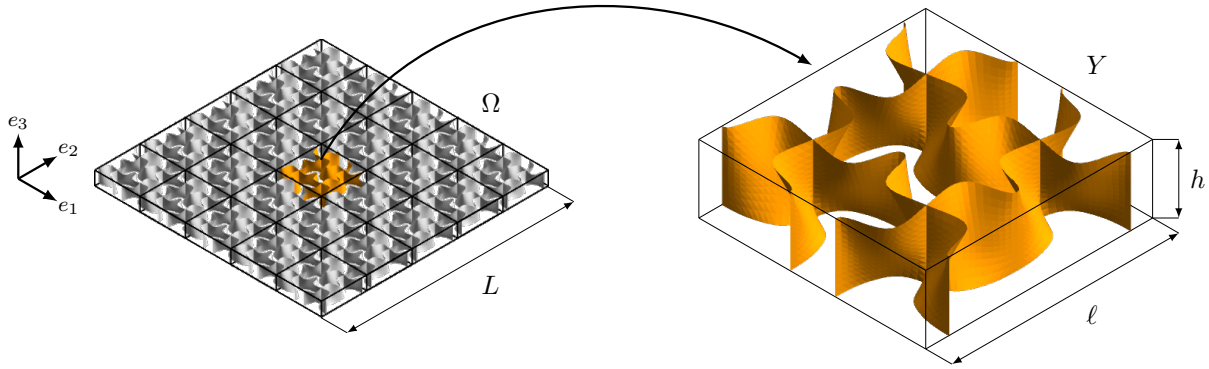

Figure 1: Architectured panel Ω with a periodic arrangement of 5×5 unit cells. The unit cells are composed of structural shells parametrised by b-spline surfaces. The thickness of the shell t is not depicted (only the mid-surface is shown). The displayed unit cell is obtained following the procedure described in section 2. It has an aspect ratio $h^* = h/\ell = 0.3$.

bendable trusses or hinges are suitable to shape three-dimensional objects with desired geometrical sizes and aspects ratios [31, 32], but due to the thin connections at the hinges, they are mechanically weak. Ribbon- and membrane-like flat structures can buckle out of plane and produce three-dimensional geometries when subject to mechanical actuation [33–35]. Lastly, bilayers sheets can morph into three-dimensional surfaces with non-zero Gaussian curvature [36, 37], but their fabrication is complex.

Most systems are paired with mechanical actuations through manual forming, boundary loading, or through the release of a pre-stretched layers. By releasing pre-stretched shape memory layers, it is possible to control the deformation in time, which is an essential feature to prevent collisions while undertaking complex morphing [38–40]. Other studies make use of pneumatic power to mechanically load the shapes [5, 41]. Alternatively, combining shape-morphing structures with multiphysics phenomena further opens up the space for various actuation mechanism. Self-actuation enables autonomous structural adaptation to changing environmental stimuli. For example, self-shaping concepts have been demonstrated in shells through hydrogel swelling [42–44], nematic-to-isotropic phase changes in liquid-crystal elastomers [45, 46], and using piezo-electric actuation [36, 47]. Multiple materials in heterogeneous lattice designs enabled unprecedented morphing capacities with complex and doubly curved shapes (*e.g.* a human face) [48]. Nevertheless, complex shapes remain difficult to achieve experimentally, as they often require advanced multi-material 3D printers with long and costly fabrication.

In this work, we propose a novel class of micro-structures consisting in a combination of undulated ribbons, parametrised using b-spline surfaces. The undulations feature an asymmetry along the height that is leveraged to obtain an extension-bending coupling (EBC) mechanism. The unit cell is tessellated periodically to generate panels with programmable morphing capabilities when subject to mechanical actuation. While single undulated ribbons do not exhibit specific coupling mechanics, we demonstrate that their interconnection starts the mechanism. We then discuss the mechanical properties of a particular of a unit cell, computing the complete elastic stiffness tensor via two-scale homogenization with thin plate theory. The range of achievable EBC ratio is then assessed with respect to the geometric parameters of the unit cell. We demonstrate that the EBC ratio is not degraded under finite strain up to 20%. Ribbon-based specimen are manufactured using a desktop fused filament fabrication 3D printer and are mechanically tested for validations. Both experiments and numerical simulations are conducted to measure the out of plane local mechanical fields. Our work distinguishes itself for the simplicity of fabrication and actuation, and for its potential applicability in material and structural systems at vastly different scales; it therefore illustrates a potential base to be harnessed in combination with responsive materials for the actuation of soft robots, compliant systems and reconfigurable structures, as alternatives to external mechanical motors, control systems and power devices.

2. Design of the unit cell

Let us consider an architectured panel occupying a plane domain Ω, of characteristic in-plane dimension L, and of height h, as sketched in Figure 1. It is a periodic or graded compound of quadrangular building blocks, referred to as *unit cells* and denoted as Y, of characteristic in-plane dimension ℓ. The unit cells consist in a network of undulated ribbons of constant thickness t creating a composite similar to open cell foams described in [49, 50]. As unit cells may be scaled to various sizes, we define a rescaled unit cell Y^* characterised by two dimensionless parameters: the unit cell aspect ratio, $h^* = h/\ell$ and the normalized thickness, $t^* = t/\ell$. The material distribution inside the cell is parametrised using multiple b-spline surfaces, *i.e.* a bivariate vector-valued piecewise rational function of degree p in the u direction and degree q in the v direction respectively:

$$\mathbf{S}(u,v) = \sum_{i=0}^{n} \sum_{j=0}^{m} N_{i,p}(u)\, N_{j,q}(v)\, \mathbf{P}_{i,j} \tag{2.1}$$

where $\mathbf{P}_{i,j}$ is a bidirectional net of control points (CP), while $N_{i,p}(u)$ and $N_{j,q}(v)$ are the b-spline basis functions [51]. The choice of the control points $\mathbf{P}_{i,j}$ is made with the aim to engender the extension bending (EBC) effect in the panel. It is realised manually, according to the following design procedure:

1. Select five filament based two-dimensional unit cells with an negative effective Poisson's ratio equally dispersed within $[-0.8, 0.]$ (see Figure 2(a)).

2. Thanks to the multiple symmetries, the parametrisation is restricted to a bundle of elementary corrugated branches, modelled as b-splines curves with five CP [51]. The global number of control points is reduced as all unit cells are sharing the end points and therefore only three independent CP per curve suffice to control the effective Poisson's ratio of each unit cell (see Figure 2(b,d)).

3. CP for each b-spline curve (from Figure 2(b)) are uniformly distributed along the thickness according to the desired height. Using the b-spline surface parametrization, ribbons are constructed as *lofted* surface, depicted in Figure 2(c) and feature a two-fold undulation: (1) an in-plane corrugation stemming from the 2-d microstructures and (2) a continuously varying profile along the height. Fixing the outermost CP for all curves ensure a resulting vertical border and permits the construction of the unit cell and of the periodic pattern by symmetry.

This ribbon-based unit cell encompasses a continuous stacking of two-dimensional shapes with varying effective Poisson's ratio. Hence, we can recover any two-dimensional unit cells that attain any effective Poisson's ratio between -0.8 and 0 by taking a slice of the micro-architectured panel at the corresponding height. We recall that materials with a negative Poisson's ratio, also called auxetics, expand transversally under a uniaxial stretching. They often derive this property from microstructural deformation mechanisms that typically involve rotations [53, 54], which can confer enhanced mechanical properties. To date, several types of auxetic materials have been reported [55–57]. This class of auxetic unit cells considered here was first reported in [52] and stems from a topology optimization with the objective to exhibit a prescribed effective Poisson's ratio over finite deformations of up to 20%. The choice to use these shapes was motivated by the following reasons: (1) In comparison with other shapes in the literature designed using topology optimization [58–60], they are featuring high geometrical simplicity (arrangement of curved beams with constant thickness t), which is suitable for design flexibility, and manufacturability. In particular, they are adapted for specific additive manufacturing technologies based for example on wire deposition, such as Fused Filament Fabrication for polymers, or Wire Arc Additive Manufacturing for metals. (2) They share a common generic configuration, which simplifies their tesselation and enables a global parametrization using design points and b-spline curves (as shown in Figure 4 in [52]). (3) They were designed to maintain their auxetic effect at finite strains. This feature confers to the panel constant EBC effect at finite strain, as it will be shown in the sequel.

Finally, let us remark that the proposed design procedure based on stacking of filament unit cells using b-splines and lofted surfaces is not restricted to the present choice, neither as in-plane geometries nor in terms of symmetries, and opens up a new direction to create shell like panels.

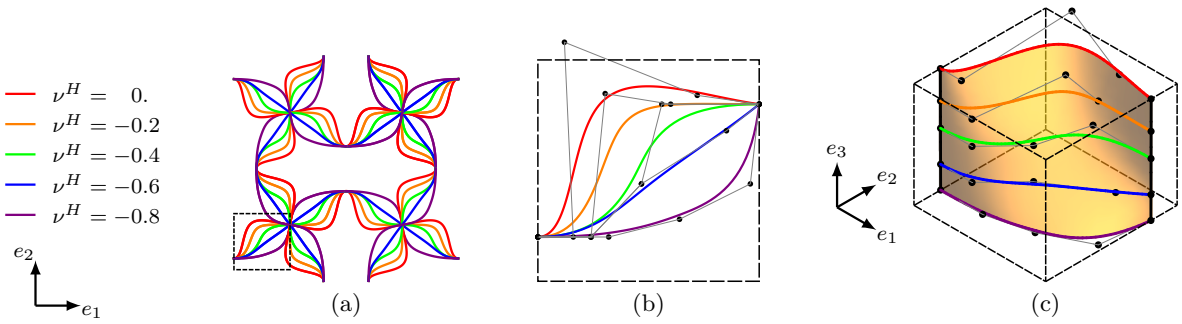

	CP1	CP2	CP3	CP4	CP5
$\nu^H = 0$	$(0.25, 0.25, 0)$	$(0.18, 0.26, 0)$	$(0.03, 0.32, 0)$	$(0.04, 0.1, 0)$	$(0, 0.1, 0)$
$\nu^H = -0.2$	$(0.25, 0.25, 0.25h^*)$	$(0.15, 0.25, 0.25h^*)$	$(0.08, 0.26, 0.25h^*)$	$(0.06, 0.1, 0.25h^*)$	$(0, 0.1, 0.25h^*)$
$\nu^H = -0.4$	$(0.25, 0.25, 0.5h^*)$	$(0.14, 0.25, 0.5h^*)$	$(0.12, 0.16, 0.5h^*)$	$(0.06, 0.1, 0.5h^*)$	$(0, 0.1, 0.5h^*)$
$\nu^H = -0.6$	$(0.25, 0.25, 0.75h^*)$	$(0.21, 0.22, 0.75h^*)$	$(0.12, 0.16, 0.75h^*)$	$(0.06, 0.1, 0.75h^*)$	$(0, 0.1, 0.75h^*)$
$\nu^H = -0.8$	$(0.25, 0.25, h^*)$	$(0.24, 0.16, h^*)$	$(0.16, 0.12, h^*)$	$(0.08, 0.1, h^*)$	$(0, 0.1, h^*)$

(d)

Figure 2: B-spline parametrisation. (a) Class of architected materials, inspired by Clausen et al. [52]. The boxed branches on the bottom left are the most basic pattern required to reconstruct the whole unit cell. (b) elementary pattern parametrised using b-spline and their control points (CP). (c) B-spline surface built upon the uniform distribution of the CP in (b) along the thickness. (d) Coordinates of the CP defining each of the five b-spline curves needed to build the surface. The value report regards a cell of characteristic length $\ell = 1$.

3. Extension bending coupling (EBC) mechanism

The extension-bending coupling (EBC) mechanism is investigated first by analysing the behaviour of a single undulated ribbon under tension in order to exhibit the particular features at the origin of the EBC effect. Then, the effective behaviour of the panel is numerically identified at small and finite strain. A parameter analysis permits to evaluate the variation of mechanical properties characterising the EBC effect against the geometrical parameters of the unit cell. Finally, the influence of a graded stiffness in the ribbon on the EBC effect is briefly discussed.

The analysis is based on finite element computations and is conducted using the solver Cast3M 2018 (`www-cast3m.cea.fr`). The parametric b-spline surfaces are triangulated by discrete Kirchhoff triangular (DKT) shell elements [61, 62] to generate a discrete shell model. The ribbon material is considered to be elastic, isotropic and quasi-incompressible, with parameters $E^0 = 0.7599\,\text{MPa}$ and $\nu^0 = 0.49$. They yield a *normalized* in-plane elastic stiffness in tension, *i.e.* $A^0_{1111} = A^0_{2222} = 1.0\,\text{MPa}$ (under plane stress assumption) which simplifies the analysis for applications under an assumption of a linear elastic behaviour.

Displacement and rotation are vector valued functions in the cartesian system of coordinates (e_1, e_2, e_3). For convenience, in-plane displacements will denote the components along e_1 or e_2, while displacements along e_3 are referred to as out of plane displacement. Meanwhile, rotations of cross sections around e_3 are denoted as in-plane rotations, while rotations around e_1 or e_2 are referred to as out of plane rotations and characterise the bending deformation of the panel.

3.1. Deformation mechanisms of undulated ribbons

In order to understand the EBC effect, we propose to compare the kinematic deformations patterns of single undulated ribbon oriented along e_1 under a uniaxial tensile load, with the deformation of the same ribbon connected with a transverse ribbon respecting the architecture of the panel. For all cases the effective strain reaches 10% and is applied assuming periodic boundary conditions and planes of symmetry as depicted for different cases in Figure 3, which resumes the computations.

For the single ribbon, computed components of rotations and displacement fields along e_3 are displayed in Figure 3(a,d). As the ribbon elongates, the initial in-plane corrugations *unfold* through a bending mechanism about the e_3 axes and align with the loading direction e_1. The bending is localized in the regions with a vertical cross-section

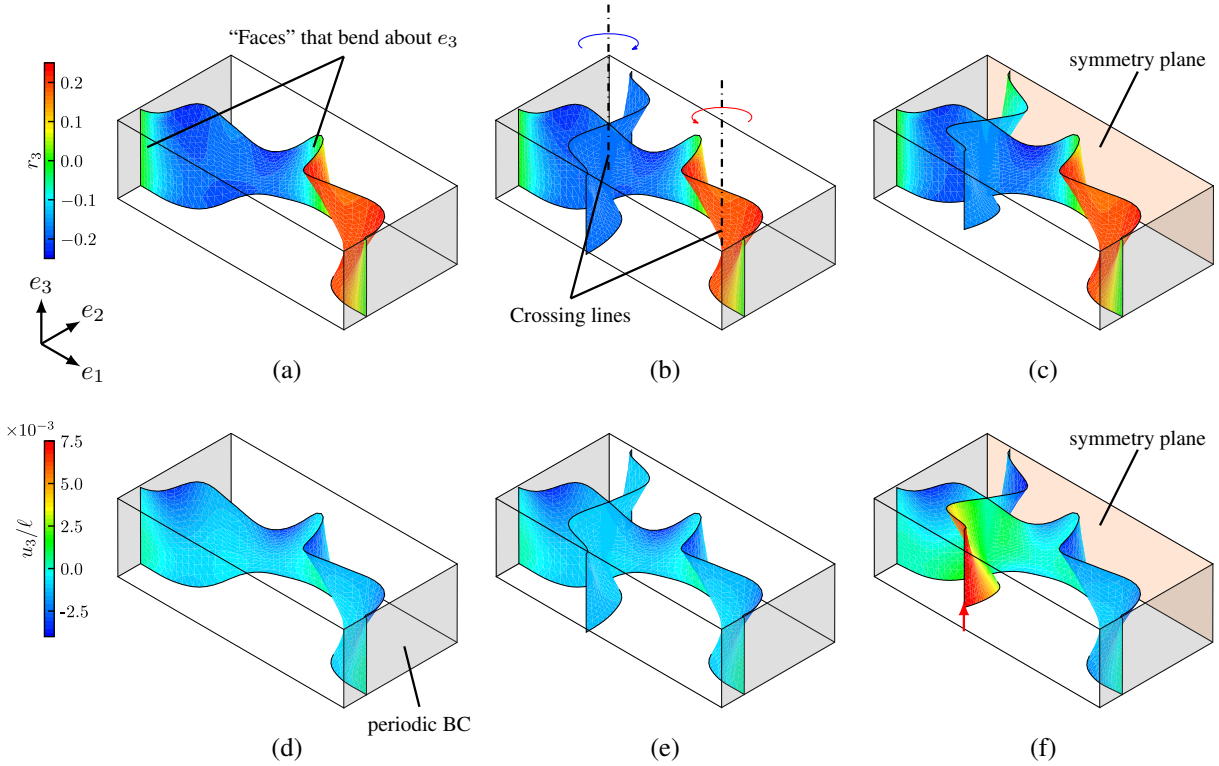

Figure 3: Numerical results on ribbon blocks subjected to periodic boundary conditions, loaded in tension up to 10% effective strain. The aspect ratio is $h^* = h/\ell = 0.3$ and the normalized thickness is $t^* = t/\ell = 0.05$. In all figures, the deformed along the direction e_3 is amplified ten times. (a-c) In-plane rotation field r_3 (about e_3) plotted as a color map on the deformed ribbon. The color bar on the left applies to the three cases. (d-f) Out of plane displacement field u_3 (normalized by ℓ) plotted as a color map on the deformed ribbon. The color bar on the left applies to the three cases. (a,d) Uniaxial response of a single undulated ribbon. (b,e) Are the same as (a,d), but we attach a transverse undulated ribbon. The free transverse ribbon undergoes a in plane rotation about the e_3 axis, but no significant out of the plane displacement is reported. (c,f) The transverse ribbon is submitted to a symmetry condition ($u_2 = 0$, $r_3 = 0$), which reveals an out of plane displacement u_3.

oriented along e_3 which exhibit an in plane rotation. These regions are denoted as "faces" that bend about e_3 in Figure 3(a)). In the zone of ribbon crossing, the displacement of the ribbon stays in-plane, with $u_3 \approx 0$, as illustrated in Figure 3(d)). Furthermore the out of plane rotations are vanishing and the in plane rotation is constant, characterising the in-plane deformation of the ribbon and the absence of bending. Next, Figure 3(b,e) exhibits the results of the tension of the same ribbon connected with a free transverse ribbon and show that the system will equally remain in-plane and will not bend out of plane. As expected, the transverse ribbon will simply rotate in plane as imposed by the crossing line of the longitudinal ribbon, as discussed before. See Figure 3(b) for details.

For connected ribbons, with an imposed symmetry boundary conditions at the extremities of the transverse ribbon, an out-of-plane bending is revealed, as shown in Figure 3(c,f). Now, upon pulling on the longitudinal ribbon, the transverse ribbons is also submitted to a bending load along e_3. As the longitudinal ribbon elongates, both in plane and out of plane bending of the transverse ribbon is observed about the e_3 and e_1 axes respectively. In other words, the longitudinal ribbon is tilted at the connection line, yielding out of plane deflection in the transverse ribbon (Figure 3(f)). We conclude that the shifting mechanism is driven by the coupled in-plane and out of plane bending occurring inside the ribbons.

3.2. From undulated ribbons to architectured unit cells

The quantitative estimation of the EBC effect can be obtained analysing the effective material behaviour, *i.e.* obtained as the ratio of the averaged stiffness and strain over the unit cells. The precise technique is defined by the two-scale homogenization method applied to periodic plates. Due to the great number of unit cells in Ω, the dimension of the

periodic cells ℓ is assumed to be much smaller than L (*i.e.* $\ell/\epsilon = O(L)$, where ϵ tends to 0), but is assumed to be comparable to h (*i.e.* $\ell = O(h)$). Furthermore, the thickness t is assumed to be much smaller than ℓ and h (so that we verify the shell assumption). In practice, we assume:

$$0.1 \leq h^* \leq 10, \qquad t^* \leq 5h^*. \tag{3.1}$$

To interpret the observed bending in terms of effective material parameters, we need to map the behaviour within the classical Kirchhoff-Love plate theory (see Appendix A for a short recall). The constitutive behaviour of a general thin plate reads:

$$\begin{bmatrix} \boldsymbol{N} \\ \boldsymbol{M} \end{bmatrix} = \begin{bmatrix} \boldsymbol{A} & \boldsymbol{B} \\ \boldsymbol{B} & \boldsymbol{D} \end{bmatrix} \begin{bmatrix} \boldsymbol{\mu} \\ \boldsymbol{\chi} \end{bmatrix} \tag{3.2}$$

where $\boldsymbol{N}$ and $\boldsymbol{M}$ are the membrane stress and bending moments per unit width. Units are: $[\boldsymbol{N}] = \text{N.m}^{-1}$ and $[\boldsymbol{M}] = \text{N}$. The plate kinematic is described by the in-plane (membrane) strains $\boldsymbol{\mu}$ and the out-of-plane curvatures $\boldsymbol{\chi}$. Units are: $[\boldsymbol{\mu}] = \text{m.m}^{-1}$ and $[\boldsymbol{\chi}] = \text{m}^{-1}$. The tensor $\boldsymbol{A}$ describes the in-plane behaviour, the tensor $\boldsymbol{D}$ describes the bending behaviour, and their coupling is expressed through the tensor $\boldsymbol{B}$. Units are: $[\boldsymbol{A}] = \text{N.m}^{-1}$, $[\boldsymbol{B}] = \text{N}$ and $[\boldsymbol{D}] = \text{N.m}$. Note that in most engineering applications, where panels feature symmetric geometry and material distribution along the thickness, normal and shear behaviour get uncoupled for the membrane part, yielding $\boldsymbol{B} = 0$.

Homogenisation of plates with periodic microstructure was first studied in [63] and [64]. A short recall on the derivation of the linearized effective equations for infinitesimal deformation of panel with periodic microstructure is provided in the Appendix B, while interested readers may refer to [65, 66] for more extended explanations. Assuming a composite panel made of two isotropic phases (material and void in this case), the constitutive behaviour for Kirchhoff-Love thin plate exhibits an orthotropic behaviour in the most general case [65], hence it reads in its component form:

$$\begin{bmatrix} \boldsymbol{A}^H & \boldsymbol{B}^H \\ \boldsymbol{B}^H & \boldsymbol{D}^H \end{bmatrix}_{(h^*,t^*)} = \left[\begin{array}{ccc|ccc} A^H_{1111} & A^H_{1122} & 0 & B^H_{1111} & B^H_{1122} & 0 \\ A^H_{1122} & A^H_{2222} & 0 & B^H_{1122} & B^H_{2222} & 0 \\ 0 & 0 & A^H_{1212} & 0 & 0 & B^H_{1212} \\ \hline B^H_{1111} & B^H_{1122} & 0 & D^H_{1111} & D^H_{1122} & 0 \\ B^H_{1122} & B^H_{2222} & 0 & D^H_{1122} & D^H_{2222} & 0 \\ 0 & 0 & B^H_{1212} & 0 & 0 & D^H_{1212} \end{array}\right] \tag{3.3}$$

Superscripts H denote an effective or homogenized quantity, defined at the macroscopic scale of the panel. For instance, the effective Young's modulus, Poisson's ratio and shear modulus are denoted as E^H, ν^H, and G^H respectively, hereinafter. In equation (3.3), the in-plane elastic moduli depend on h mainly according to $1/h$, the flexural moduli depend on h mainly according to $1/h^3$.

Example of effective plate elastic stiffness tensor. In a rescaled unit cell with $h^* = 0.3$ and $t^* = 0.05$, the material volume fraction is of 26.7% and its constitutive tensor reads:

$$\begin{bmatrix} \boldsymbol{A}^H & \boldsymbol{B}^H \\ \boldsymbol{B}^H & \boldsymbol{D}^H \end{bmatrix}_{(0.3,0.05)} = 10^{-3} \left[\begin{array}{ccc|ccc} 4.18 & -1.89 & 0. & 0.01 & 0.45 & 0. \\ -1.89 & 4.18 & 0. & 0.45 & 0.01 & 0. \\ 0. & 0. & 0.74 & 0. & 0. & 0.44 \\ \hline 0.01 & 0.45 & 0. & 1.05 & -0.14 & 0. \\ 0.45 & 0.01 & 0. & -0.14 & 1.05 & 0. \\ 0. & 0. & 0.44 & 0. & 0. & 1.02 \end{array}\right] \tag{3.4}$$

The matrices $\boldsymbol{A}^H$, $\boldsymbol{B}^H$ and $\boldsymbol{D}^H$ are symmetric and exhibits an *quadratic* symmetry, *i.e.* the plate has the same tensile (respectively bending) stiffness along e_1 and e_2. $A^H_{1122} < 0$ indicates an effective auxetic behaviour of the unit cell. An underlying effect accounted by $D^H_{1122} < 0$ is to undergo synclastic curvatures [67], *i.e.* shifting from flat to a dome shape under bending. The main non-vanishing coupling stiffness is B^H_{1122}. It links the in-plane stress along e_1 (respectively e_2) to the transverse curvature about e_1 (respectively e_2). This suggests that the EBC effect exists primarily between the longitudinal in plane displacements and the out of plane bending curvature, which is in agreement with

the concept of overlaying profiles with varying Poisson's ratios. We also note the presence of a coupling between the shears B^H_{1212}.

The elastic moduli, $A^H_{\alpha\beta\gamma\delta}$, $B^H_{\alpha\beta\gamma\delta}$ and $D^H_{\alpha\beta\gamma\delta}$ can be expressed in terms of materials parameters E^H and ν^H. We further introduce the effective longitudinal extension - transverse bending coupling ratio, referred in the sequel as to EBC ratio and denoted by β^H.

$$E^H = \frac{1}{h^*} A^H_{1111}\left(1 - \left(\frac{A^H_{1122}}{A^H_{1111}}\right)^2\right); \qquad \nu^H = \frac{A^H_{1122}}{A^H_{1111}}; \qquad \beta^H = \frac{1}{h}\frac{B^H_{1122}}{A^H_{1111}} \tag{3.5}$$

Note. the division by h is here to obtain a dimensionless quantify.

3.3. *Influence of h^* and t^**

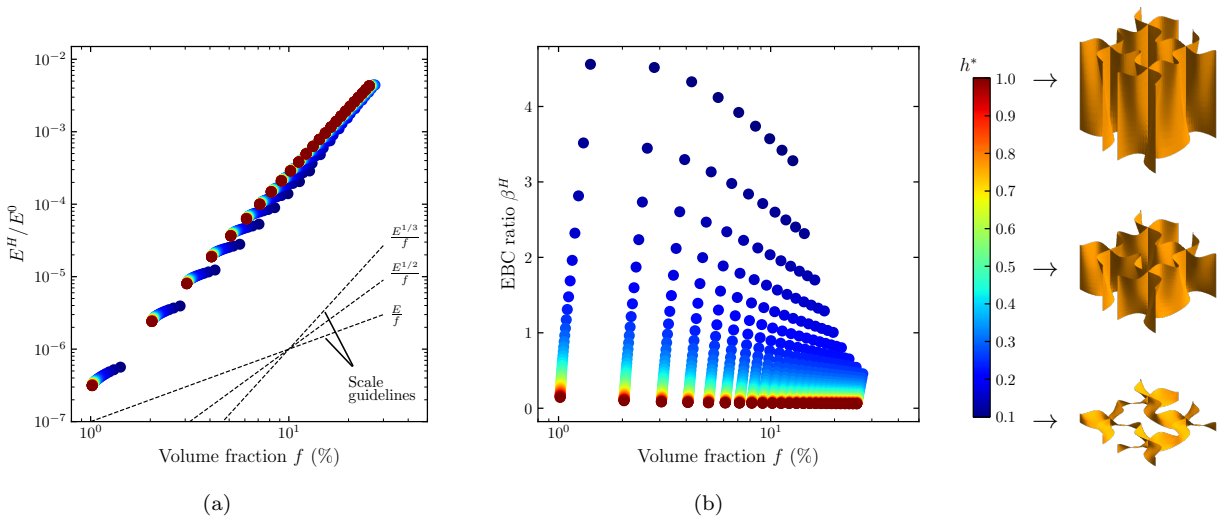

(a) (b)

Figure 4: Parameter analysis with respect to h^* and t^*. Material property charts (a) Normalized effective Young's modulus E^H/E^0 versus material volume fraction f. Performances of these architectured materials can be mapped in already existing material property charts, like in [68], for further comparisons with other materials. (b) EBC ratio β^H from equation (3.5) versus material volume fraction. The color bar on the right applies for both plots. The unit cells associated to specific heights are also depicted.

Next, we investigate the variations of the effective stiffness of the unit cell, as a function of the aspect ratio of the panel h^*, or the normalized thickness of the ribbons t^*. The analysis is numerically performed by varying: (i) h^* from 0.1 to 1 with a step of 0.02 and; (ii) t^* from 0.002 to 0.05 with a step of 0.002, provided both h^* and t^* satisfy the inequalities (3.1). The results are reported against the material volume fraction f of the cell, which facilitates comparisons with standard materials property charts [68]. Estimations from the three-dimensional numerical models indicate that f is depending linearly to t^*, while it is almost unaltered by h^*.

Investigation under small strain assumption. The distribution of effective Young's modulus E^H, normalised by the base material modulus E^0, is mapped against the volume fraction f for different values of h^* in Figure 4(a). It is proportional to the cube of the volume fraction. Conversely, its dependence on the aspect ratio h^* is much less pronounced, *i.e.* a unit cell of aspect ratio h^* is about as stiff as a pile of n unit cells of aspect ratio h^*/n. Macroscopically, this ribbon based unit cell is highly compliant, the Young's modulus E^H being from two to six orders of magnitude lower than its bulk equivalent (see base elastic coefficients in section 3 above). Next, the distribution of the EBC ratio β^H (Figure 4(b)) indicates the effect is stronger for smaller aspect ratios h^*. Moreover, we report that for $h^* > 0.25$, the EBC ratio β^H is almost independent from the normalized thickness t^*, while for $h^* < 0.2$, the EBC ratio is affected by t^*. All things considered, E^H and β^H can be tailored relatively independently. On a side note, the effective Poisson's ratio ν^H does not depend particularly depend on h^* and t^*. Its average value ≈ -0.4 matches the expectations considering the overlaying of initial two-dimensional profiles with an effective Poisson's ratio in range between -0.8 and 0.

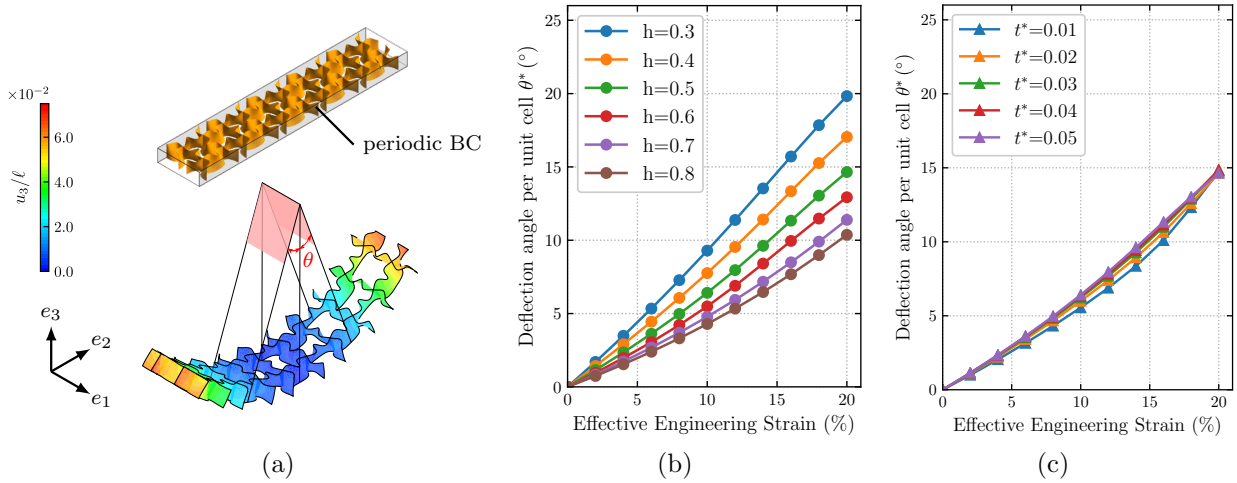

Figure 5: (a) Deformed configuration under tension along e_1 up to 20% effective strain, with imposed periodic BC at front and rear faces. The deflection angle θ^* per unit cell induced in the direction perpendicular to the loading is illustrated. For different loading values, nodes at the two lateral boundary of the central cell (normal vectors to the faces are $-e_1$ and e_1) form two planes (depicted in pink). A least square fit permits to calculate the cartesian equation of these two planes, which in turn yields the deflection angle θ^*. (b) Evolution of θ^* against the longitudinal effective engineering strain. t^* is set at 0.05, h^* is varying. (c) Same as (b), but now h^* is set at 0.5, t^* is varying.

Uniaxial extension at finite strain. To characterize the out of plane capacities of the unit cell at finite strain up to 20% under uniaxial tension, a strip of 5 unit cells was loaded using periodic boundary conditions along the transverse direction of the strip, while longitudinal direction was traction free. Several characteristics of the transverse deflection angle per unit cell θ^* are displayed in Figure 5. In particular, Figure 5(a), represents the deformed strip of unit cells and the definition of the transverse deflection angle θ^*. The EBC effect as function of h^*, illustrated through the evolution of the transverse deflection angle as a function of engineering strain is exhibited in Figure 5(b,c). However, for a fixed value of $h^* = 0.5 > 0.25$, θ^* is almost unaffected by t^* as shown in Figure 5(c). Similar to [52], one can equally remark that the evolution of the deflection angle with respect to the engineering strain follows a linear trend, which indicates that the EBC ratio remains constant for deformations up to 20%.

3.4. Influence of a varying stiffness along the height

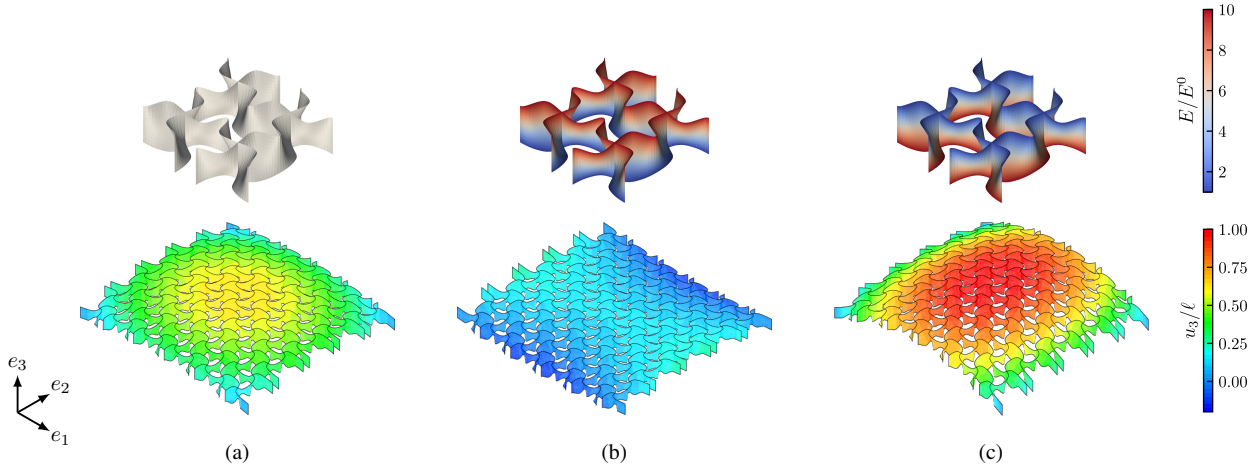

Figure 6: Deformed panel loaded in uniaxial tension up to 10% effective strain. The aspect ratio here is $h^* = h/\ell = 0.3$ and the normalized thickness is $t^* = t/\ell = 0.05$. (a) Uniform Young's modulus. (b) Increasing Young's modulus along the panel height. (c) Decreasing Young's modulus along the panel's height.

A literature survey, see [69] and the references within, show that EBC effects in panels can be triggered in porous panels, provided the porosity density varies through thickness. Varying the materials properties along the thickness implies varying the elasticity properties or equivalently the thickness of the ribbons. As expected, a variation of the normalised Young's modulus E^H/E^0 along the panel's height h^* by a factor ranging from 1 to 10 engenders visible EBC effects. Figure 6 presents a comparison of the deflection pattern of three panel comprising 5×5 unit cell of subject to an uniaxial tensile loading of 10% with (a) homogeneous, (b) increasing, (c) decreasing Young's modulus with height, respectively. The expected dome-shape out of plane defection of the panel with a uniform E^H over the ribbons, is amplified for a decreasing Young's modulus with height. However, an increasing Young's modulus with height will trigger a a novel saddle-shape deformation of the panel. This example reveals that a variation of the material properties of the ribbons add a novel shape shifting dimension to the family of ribbon based unit cells.

4. Analysis of fabricated polymer panels

4.1. Additive manufacturing

Specimens of architectured panels with ribbon-based unit cells have been additively manufactured with fused filament fabrication technology (FFF) using a commercial Ultimaker 3D printer and a thermoplastic polyurethane filament TPU 95A with a diameter 0.4mm[1]. The choice of TPU 95A was motivated by its compliant nature and capacity to undergo large deformations, i.e. > 20% strain without breaking.

The 3D volume model of the unit cell was obtained by computing the normal vector field of the b-spline surface and by shifting it along the normal to create the upper and lower surfaces. The upper and lower surfaces are then completed with the bottom and top boundary a closed envelope. The complete envelope is triangulated exported as a watertight STL mesh. The specimen is a periodic array of 5×5 unit cells with $h^* = 0.3$ and $t^* = 0.05$. The dimension of the unit cell is $\ell = 16$ mm and conducts thus to a panel with $L = 80$ mm of dimensions 80 mm×80 mm×4.8 mm. The generated pattern was completed by a series of rings to ensure the fixing within the testing machine. The non-conventional ring fixture and the underlying boundary conditions is discussed in the next section.

4.2. Mechanical testing

The experiments are performed on an Instron 10 kN universal testing machine, under displacement control at a quasi-static strain rate $\dot{\varepsilon} = 0.125\,\mathrm{min}^{-1}$ up to 20% effective engineering strain. Each mechanical test is recorded using a high-resolution digital camera (JAI Spark SP-20000-USB camera with a resolution of 5120×3840 pixels equipped with a Tokina AT-X Pro 100 mm F2.8 macro lens), mounted on a perpendicular axis with respect to the plane of the specimen. Using a inclined mirror, we capture the front and lateral view of the specimen in each picture, as shown in Figure 7. Using an in-built computer program, 8-bit gray scale sub-images were stored every second during the loading. The out of plane displacement u_3 at the tip of the ribbon identified in the lateral mirror view is measured 2-d point tracking method (Tracker software: `https://physlets.org/tracker/`) from the image sequence. A white grid is added to the sample to facilitate the optical measurements.

Early stage tests performed on specimens fixed by standard hard clamp montages (not shown here) gave unsatisfactory results. More precisely, the resulting out of plane displacement field was below the expected results of the computations with periodic boundary conditions displayed in Figure 5, indicating that the 5×5 array specimen, with clamped boundaries does not approximate the results of an infinite periodic domain. Standard hard clamp montage are a dead load and induce induce over-constrained boundary conditions, preventing the out of the plane deformation of the specimen. A way to relax the the encastred boundary conditions of the clamps was to add an intermediate fixing comprising a rod and a series of rings which add additional degrees of freedom at the boundary of the specimen. Similar specimen fixing were attempted in previous works in the literature [30, 32, 70].

[1] Characteristics of TPU 95A filaments are provided here: https://support.ultimaker.com/hc/en-us/sections/360003556679

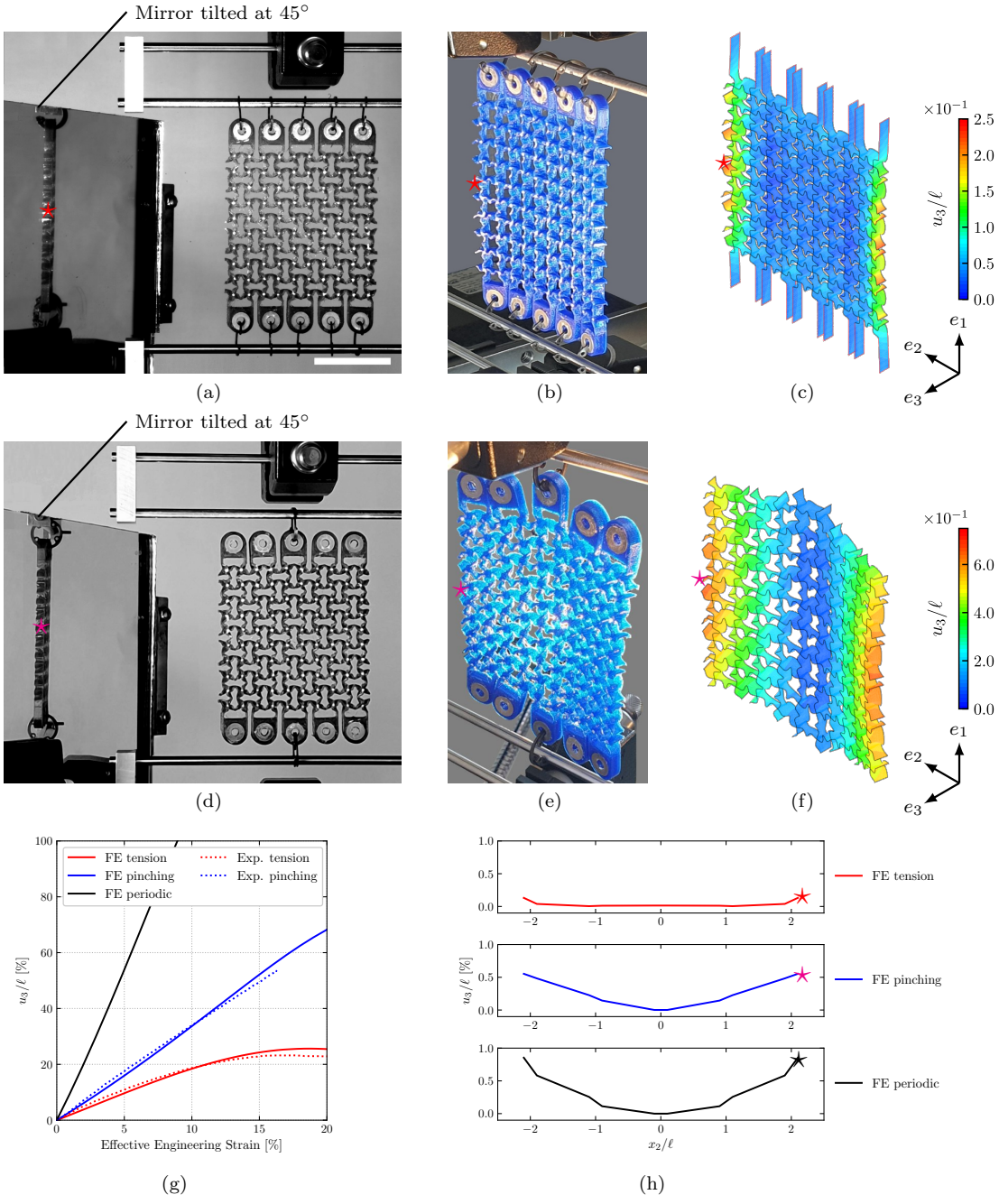

Figure 7: Comparison of experimental and computed results. Extension test: (a) experimental setup, (b) observed specimen at maximal extension $\varepsilon^H = 20\%$ (c) computed relative out of plane displacement u_3/ℓ. Extension by concentrated load, *i.e;* pinching test: (d) experimental setup, (e) observed specimen at maximal extension $\varepsilon^H = 16\%$ (f) computed relative out of plane displacement u_3/ℓ. (g) Comparison of the evolution of the out of plane displacement at the measurement point (indicated by $\star$ in the images). (h) Comparison between the numerical deformed cross-sections at mid specimen.

Extension with customized fixture. The specimen is hung between the clamps at both extremities by metallic rings to steel rods in a curtain-like fashion, as shown in Figure 7. Prior to the montage, the steel rods were covered in oil to reduce the frictions with the rings. Although this fixture accommodates lateral expansions and rotations of the specimens undergoing tensile loads, it is worth noting that it introduces uncertainties, due to the unknown friction between the rings and the rods. This limitation is addressed by analysing two distinct types of boundary conditions in the numerical simulations associated to this tensile test: (i) free traction in the corresponding directions, neglecting friction and are compatible with periodic boundary conditions or (ii) adding stiff pinned rods at the extremity of the specimen, which permit an out-of-plane tilt without a transversal slide and are appropriate for the extension test discussed next.

The results of the extension experiment are depicted in Figure 7. The different sub-figures represent: (a) the experimental setup, (b) the observed specimen during the experiment at maximal extension, *i.e.* 20% effective strain and (c) the computed relative out of plane displacement field u_3/ℓ plotted on the deformed mesh assuming the boundary conditions (ii). The results present en excellent match between computations under experimental boundary conditions and experimental measurements as a deformation pattern and quantitatively when the displacements are compared at a given point, see red curves in subfigure (g). Moreover, a saturation saturation of the out-of-plane displacement at about 15% engineering strain is observed on both experiments and computations. If the comparison between experiments and computation is satisfactory, they both exhibit an important discrepancy with the behaviour of the structure under perfect periodic boundary condition, both in the deformation pattern and quantitatively as the out-of-plane displacement is increased by a factor of six when compared with the tensile experiment.

Extension by concentrated force, referred to as pinching test. The results of the pinching experiment, where the extension is applied only on the central ring are represented in Figure 7. The different sub-figures represent as before: (d) the experimental setup, (e) the observed specimen during the experiment at maximal extension, *i.e.* 16% effective strain and (c) the computed relative out of plane displacement field u_3/ℓ plotted on the deformed mesh. As before one can remark an excellent match between experiments and computations, both in terms of deformation pattern and quantitatively when the displacements are compared at a given point, see blue curves in subfigure (g). The results exhibit on the one hand side a three-fold increase of the out-of-plane displacement when compared with the previous extension experiment and on the other hand side present a linear increase of the out of plane displacement with applied strain without the saturation plateau of the previous extension experiment.

Finally, Figure 7(h) presents the computed out-plane displacements of a nodal line at the center of the specimen, transverse to the extension direction. The comparison of the shapes shows that the extension experiment does not reach an important curvature at the center and that the out-of-displacement is concentrated at the boundaries, which is in contrast with the extension by a concentrate force where a significative curvature at the center is obtained. Moreover the pinching experiment and the periodic boundary condition reach similar curvatures at the center of the specimen and that the quantitative difference of the measured out of plane experiment is due only in the deformation patterns of the last cell at the boundary of the specimens where the boundary conditions differ.

5. Conclusion and perspectives

In this paper, we designed a new class of micro-structures composed of undulated ribbon lattice. These micro-structures can be arranged periodically to obtain panels exhibiting a bending deflection when submitted to in-plane tension, hence producing the EBC effect. For a prescribed shape of the of the unit cell, *i.e.* shape of the ribbons and intersections, the aspect ratio of the ribbons and their thickness, tailor the various elastic coefficients, like stiffness or EBC ratio.

Our work expands the spectrum of shape-morphing structures manufactured with a single material, and it indicates an approach that could be used to produce morphing and deployable structures for a wide range of scales. While the shapes we have obtained are relatively simple, similar principles could be extended to different families of materials, and could be coupled to parametric optimization (using b-spline) and inverse-design strategies to obtain more extreme shapes. This type of analysis would also permit to shed light on the set of realizable moduli using undulated ribbon-based structures (refer for analogy to the study of [71] regarding laminates).

The geometric parameters of proposed ribbon based architectures can be tuned to create panels with controlled EBC effect and combined with active materials like swelling gels, piezo-electrics, nematic elastomers, LCE's, in the different layers of the unit cell to trigger the shape shifting effect by external stimuli.

Acknowledgements

F. A. acknowledges the support of the French doctoral fellowship "Contrat Doctoral Spécifique pour Normalien". The specimens have been printed at the Drahi-X Novation Center from Ecole polytechnique during the Summer, 2020. The authors acknowledge Aline Becq and Gareth Paterson for valuable input regarding the printing aspects and Giovanni Frascella, for his help with the testing phase.

References

[1] K. Oliver, A. Seddon, R. S. Trask, Morphing in nature and beyond: a review of natural and synthetic shape-changing materials and mechanisms, J. Mater. Sci. 51 (24) (2016) 10663–10689. doi:10.1007/s10853-016-0295-8.

[2] Z. X. Khoo, J. E. M. Teoh, Y. Liu, C. K. Chua, S. Yang, J. An, K. F. Leong, W. Y. Yeong, 3D printing of smart materials: A review on recent progresses in 4D printing, Virtual Phys. Prototyp. 10 (3) (2015) 103–122. doi:10.1080/17452759.2015.1097054.

[3] R. Guseinov, E. Miguel, B. Bickel, CurveUps : Shaping objects from flat plates with tension-actuated curvature, ACM Trans. Graph. 36 (4) (2017) 1–12. doi:10.1145/3072959.3073709.

[4] L. Malomo, J. Pérez, E. Iarussi, N. Pietroni, E. Miguel, P. Cignoni, B. Bickel, Flexmaps: Computational design of flat flexible shells for shaping 3d objects, ACM Trans. Graph. 37 (6) (2018) 1–14. doi:10.1145/3272127.3275076.

[5] A. Rafsanjani, Y. Zhang, B. Liu, S. M. Rubinstein, K. Bertoldi, Kirigami skins make a simple soft actuator crawl, Sci. Robot. 3 (15) (2018) eaar7555. doi:10.1126/scirobotics.aar7555.

[6] A. Kotikian, C. McMahan, E. C. Davidson, J. M. Muhammad, R. D. Weeks, C. Daraio, J. A. Lewis, Untethered soft robotic matter with passive control of shape morphing and propulsion, Sci. Robot. 4 (33) (2019) eaax7044. doi:10.1126/scirobotics.aax7044.

[7] A. A. Bauhofer, S. Krödel, J. Rys, O. R. Bilal, A. Constantinescu, C. Daraio, Harnessing photochemical shrinkage in direct laser writing for shape morphing of polymer sheets, Adv. Mater. 29 (42) (2017) 1703024. doi:10.1002/adma.201703024.

[8] T. Chen, O. R. Bilal, K. Shea, C. Daraio, Harnessing bistability for directional propulsion of soft, untethered robots, Proc. Natl. Acad. Sci. U.S.A. 115 (22) (2018) 5698–5702. doi:10.1073/pnas.1800386115.

[9] C. L. Randall, E. Gultepe, D. H. Gracias, Self-folding devices and materials for biomedical applications, Trends Biotechnol. 30 (3) (2012) 138–146. doi:10.1016/j.tibtech.2011.06.013.

[10] M. Cianchetti, T. Ranzani, G. Gerboni, T. Nanayakkara, K. Althoefer, P. Dasgupta, A. Menciassi, Soft robotics technologies to address shortcomings in today's minimally invasive surgery: The STIFF-FLOP approach, Soft Robot. 1 (2) (2014) 122–131. doi:10.1089/soro.2014.0001.

[11] S. Daynes, P. M. Weaver, Review of shape-morphing automobile structures: concepts and outlook, Proc. Inst. Mech. Eng. D 227 (11) (2013) 1603–1622. doi:10.1177/0954407013496557.

[12] R. M. Ajaj, C. S. Beaverstock, M. I. Friswell, Morphing aircraft: The need for a new design philosophy, Aerosp. Sci. Technol. 49 (2016) 154–166. doi:10.1016/j.ast.2015.11.039.

[13] S. Jacobs, C. Coconnier, D. D. Maio, F. Scarpa, M. Toso, J. Martinez Iglesias, Deployable auxetic shape memory alloy cellular antenna demonstrator: design, manufacturing and modal testing, Smart. Mater. Struct. 21 (7) (2012) 075013. doi:10.1088/0964-1726/21/7/075013.

[14] M. Arya, N. Lee, S. Pellegrino, Ultralight structures for space solar power satellites, in: 3rd AIAA Spacecraft Structures Conference, 2016, p. 1950. doi:10.2514/6.2016-1950.

[15] T. Chen, O. R. Bilal, R. Lang, C. Daraio, K. Shea, Autonomous deployment of a solar panel using elastic origami and distributed shape-memory-polymer actuators, Phys. Rev. Appl. 11 (6). doi:10.1103/physrevapplied.11.064069.

[16] E. MacDonald, R. Wicker, Multiprocess 3D printing for increasing component functionality, Science 353 (6307) (2016) aaf2093–aaf2093. doi:10.1126/science.aaf2093.

[17] R. L. Truby, J. A. Lewis, Printing soft matter in three dimensions, Nature 540 (7633) (2016) 371–378. doi:10.1038/nature21003.

[18] X. Kuang, D. J. Roach, J. Wu, C. M. Hamel, Z. Ding, T. Wang, M. L. Dunn, H. J. Qi, Advances in 4D printing: Materials and applications, Adv. Funct. Mater. 29 (2) (2018) 1805290. doi:10.1002/adfm.201805290.

[19] S. Shan, S. H. Kang, Z. Zhao, L. Fang, K. Bertoldi, Design of planar isotropic negative Poisson's ratio structures, Extreme Mech. Lett. 4 (2015) 96–102. doi:10.1016/j.eml.2015.05.002.

[20] Y. Tang, J. Yin, Design of cut unit geometry in hierarchical kirigami-based auxetic metamaterials for high stretchability and compressibility, Extreme Mech. Lett. 12 (2017) 77–85. doi:10.1016/j.eml.2016.07.005.

[21] L. Mizzi, E. Salvati, A. Spaggiari, J.-C. Tan, A. M. Korsunsky, Highly stretchable two-dimensional auxetic metamaterial sheets fabricated via direct-laser cutting, Int. J. Mech. Sci. 167 (2020) 105242. doi:10.1016/j.ijmecsci.2019.105242.

[22] Z. Wei, Z. Guo, L. H. Dudte, H. Liang, L. Mahadevan, Geometric mechanics of periodic pleated origami, Phys. Rev. Lett. 110 (21). doi:10.1103/physrevlett.110.215501.

[23] E. T. Filipov, T. Tachi, G. H. Paulino, Origami tubes assembled into stiff, yet reconfigurable structures and metamaterials, Proc. Natl. Acad. Sci. U.S.A. 112 (40) (2015) 12321–12326. doi:10.1073/pnas.1509465112.

[24] J. T. B. Overvelde, T. A. de Jong, Y. Shevchenko, S. A. Becerra, G. M. Whitesides, J. C. Weaver, C. Hoberman, K. Bertoldi, A three-dimensional actuated origami-inspired transformable metamaterial with multiple degrees of freedom, Nat. Commun. 7 (1). doi:10.1038/ncomms10929.
[25] E. D. Demaine, T. Tachi, Origamizer: A practical algorithm for folding any polyhedron, in: 33rd International Symposium on Computational Geometry (SoCG 2017), Schloss Dagstuhl - Leibniz-Zentrum fuer Informatik GmbH, Wadern/Saarbruecken, Germany, 2017, pp. 34:1–34:16. doi:10.4230/LIPICS.SOCG.2017.34.
[26] S. J. P. Callens, A. A. Zadpoor, From flat sheets to curved geometries: Origami and kirigami approaches, Mater. Today 21 (3) (2018) 241–264. doi:10.1016/j.mattod.2017.10.004.
[27] M. Konaković, K. Crane, B. Deng, S. Bouaziz, D. Piker, M. Pauly, Beyond developable: Computational design and fabrication with auxetic materials, ACM Trans. Graph. 35 (4) (2016) 1–11. doi:10.1145/2897824.2925944.
[28] A. Rafsanjani, K. Bertoldi, Buckling-induced kirigami, Phys. Rev. Lett. 118 (8). doi:10.1103/physrevlett.118.084301.
[29] G. P. T. Choi, L. H. Dudte, L. Mahadevan, Programming shape using kirigami tessellations, Nat. Mater. 18 (9) (2019) 999–1004. doi:10.1038/s41563-019-0452-y.
[30] R. M. Neville, F. Scarpa, A. Pirrera, Shape morphing kirigami mechanical metamaterials, Sci. Rep. 6 (1). doi:10.1038/srep31067.
[31] M. Konaković-Luković, J. Panetta, K. Crane, M. Pauly, Rapid deployment of curved surfaces via programmable auxetics, ACM Trans. Graph. 37 (4) (2018) 1–13. doi:10.1145/3197517.3201373.
[32] P. Celli, C. McMahan, B. Ramirez, A. Bauhofer, C. Naify, D. Hofmann, B. Audoly, C. Daraio, Shape-morphing architected sheets with non-periodic cut patterns, Soft Matter 14 (48) (2018) 9744–9749. doi:10.1039/c8sm02082e.
[33] J. Chopin, A. Kudrolli, Helicoids, wrinkles, and loops in twisted ribbons, Phys. Rev. Lett. 111 (17). doi:10.1103/physrevlett.111.174302.
[34] S. Xu, Z. Yan, K.-I. Jang, W. Huang, H. Fu, J. Kim, Z. Wei, M. Flavin, J. McCracken, R. Wang, A. Badea, Y. Liu, D. Xiao, G. Zhou, J. Lee, H. U. Chung, H. Cheng, W. Ren, A. Banks, X. Li, U. Paik, R. G. Nuzzo, Y. Huang, Y. Zhang, J. A. Rogers, Assembly of micro/nanomaterials into complex, three-dimensional architectures by compressive buckling, Science 347 (6218) (2015) 154–159. doi:10.1126/science.1260960.
[35] P. Celli, A. Lamaro, C. McMahan, P. Bordeenithikasem, D. C. Hofmann, C. Daraio, Compliant morphing structures from twisted bulk metallic glass ribbons, J. Mech. Phys. Solids 145 (2020) 104129. doi:10.1016/j.jmps.2020.104129.
[36] M. Gude, W. A. Hufenbach, Design of novel morphing structures based on bistable composites with piezoceramic actuators, Mech. Compos. Mater. 42 (4) (2006) 339–346. doi:10.1007/s11029-006-0043-2.
[37] W. M. van Rees, E. Vouga, L. Mahadevan, Growth patterns for shape-shifting elastic bilayers, Proc. Natl. Acad. Sci. U.S.A. 114 (44) (2017) 11597–11602. doi:10.1073/pnas.1709025114.
[38] S. M. Felton, M. T. Tolley, E. Demaine, D. Rus, R. J. Wood, A method for building self-folding machines, Science 345 (6197) (2014) 644–646. doi:10.1126/science.1252610.
[39] Y. Mao, K. Yu, M. S. Isakov, J. Wu, M. L. Dunn, H. J. Qi, Sequential self-folding structures by 3D printed digital shape memory polymers, Sci. Rep. 5 (1). doi:10.1038/srep13616.
[40] R. Guseinov, C. McMahan, J. Pérez, C. Daraio, B. Bickel, Programming temporal morphing of self-actuated shells, Nat. Commun. 11 (1). doi:10.1038/s41467-019-14015-2.
[41] E. Siéfert, E. Reyssat, J. Bico, B. Roman, Bio-inspired pneumatic shape-morphing elastomers, Nat. Mater. 18 (1) (2018) 24–28. doi:10.1038/s41563-018-0219-x.
[42] J.-H. Na, A. A. Evans, J. Bae, M. C. Chiappelli, C. D. Santangelo, R. J. Lang, T. C. Hull, R. C. Hayward, Programming reversibly self-folding origami with micropatterned photo-crosslinkable polymer trilayers, Adv. Mater. 27 (1) (2014) 79–85. doi:10.1002/adma.201403510.
[43] J. Liu, T. Gu, S. Shan, S. H. Kang, J. C. Weaver, K. Bertoldi, Harnessing buckling to design architected materials that exhibit effective negative swelling, Adv. Mater. 28 (31) (2016) 6619–6624. doi:10.1002/adma.201600812.
[44] A. S. Gladman, E. A. Matsumoto, R. G. Nuzzo, L. Mahadevan, J. A. Lewis, Biomimetic 4d printing, Nat. Mater. 15 (4) (2016) 413–418. doi:10.1038/nmat4544.
[45] A. Kotikian, R. L. Truby, J. W. Boley, T. J. White, J. A. Lewis, 3D printing of liquid crystal elastomeric actuators with spatially programed nematic order, Adv. Mater. 30 (10) (2018) 1706164. doi:10.1002/adma.201706164.
[46] P. Plucinsky, B. A. Kowalski, T. J. White, K. Bhattacharya, Patterning nonisometric origami in nematic elastomer sheets, Soft Matter 14 (16) (2018) 3127–3134. doi:10.1039/c8sm00103k.
[47] J. Boddapati, S. Mohanty, R. K. Annabattula, An analytical model for shape morphing through combined bending and twisting in piezo composites, Mech. Mater. 144 (2020) 103350. doi:10.1016/j.mechmat.2020.103350.
[48] J. W. Boley, W. M. van Rees, C. Lissandrello, M. N. Horenstein, R. L. Truby, A. Kotikian, J. A. Lewis, L. Mahadevan, Shape-shifting structured lattices via multimaterial 4d printing, Proc. Natl. Acad. Sci. U.S.A. 116 (42) (2019) 20856–20862. doi:10.1073/pnas.1908806116.
[49] L. J. Gibson, M. F. Ashby, The mechanics of three-dimensional cellular materials, Proc. Math. Phys. Eng. Sci. 382 (1782) (1982) 43–59. doi:10.1098/rspa.1982.0088.
[50] M. F. Ashby, The properties of foams and lattices, Philos. Trans. Royal Soc. A 364 (1838) (2005) 15–30. doi:10.1098/rsta.2005.1678.
[51] L. Piegl, W. Tiller, The NURBS Book, Springer Berlin Heidelberg, 1997. doi:10.1007/978-3-642-59223-2.
[52] A. Clausen, F. Wang, J. S. Jensen, O. Sigmund, J. A. Lewis, Topology optimized architectures with programmable Poisson's ratio over large deformations, Adv. Mater. 27 (37) (2015) 5523–5527. doi:10.1002/adma.201502485.
[53] R. S. Lakes, Deformation mechanisms in negative Poisson's ratio materials: structural aspects, J. Mater. Sci. 26 (9) (1991) 2287–2292. doi:10.1007/bf01130170.
[54] K. E. Evans, A. Alderson, Auxetic materials: Functional materials and structures from lateral thinking!, Adv. Mater. 12 (9) (2000) 617–628. doi:10.1002/(sici)1521-4095(200005)12:9<617::aid-adma617>3.0.co;2-3.
[55] W. Yang, Z.-M. Li, W. Shi, B.-H. Xie, M.-B. Yang, Review on auxetic materials, J. Mater. Sci. 39 (10) (2004) 3269–3279. doi:10.1023/b:jmsc.0000026928.93231.e0.
[56] J. N. Grima, A. Alderson, K. E. Evans, Auxetic behaviour from rotating rigid units, Phys. Status Solidi B 242 (3) (2005) 561–575. doi:

10.1002/pssb.200460376.
[57] G. N. Greaves, A. L. Greer, R. S. Lakes, T. Rouxel, Poisson's ratio and modern materials, Nat. Mater. 10 (11) (2011) 823–837. doi:10.1038/nmat3134.
[58] J. Gao, H. Li, Z. Luo, L. Gao, P. Li, Topology optimization of micro-structured materials featured with the specific mechanical properties, Int. J. Comput. Methods (2018) 1850144doi:10.1142/s021987621850144x.
[59] G. Zhang, K. Khandelwal, Computational design of finite strain auxetic metamaterials via topology optimization and nonlinear homogenization, Comput. Methods Appl. Mech. Eng. 356 (2019) 490–527. doi:10.1016/j.cma.2019.07.027.
[60] F. Agnelli, A. Constantinescu, G. Nika, Design and testing of 3d-printed micro-architectured polymer materials exhibiting a negative Poisson's ratio, Continuum Mech. Thermodyn. 32 (2) (2020) 433–449. doi:10.1007/s00161-019-00851-6.
[61] K.-J. Bathe, E. Dvorkin, L. W. Ho, Our discrete-Kirchhoff and isoparametric shell elements for nonlinear analysis—an assessment, Comput. Struct. 16 (1-4) (1983) 89–98. doi:10.1016/0045-7949(83)90150-5.
[62] D. G. Talaslidis, I. I. Sous, A discrete Kirchhoff triangular element for the analysis of thin stiffened shells, Comput. Struct. 43 (4) (1992) 663–674. doi:10.1016/0045-7949(92)90507-v.
[63] D. Caillerie, J.-C. Nedelec, Thin elastic and periodic plates, Math. Methods Appl. Sci. 6 (1) (1984) 159–191. doi:10.1002/mma.1670060112.
[64] R. V. Kohn, M. Vogelius, A new model for thin plates with rapidly varying thickness, Int. J. Solids Struct. 20 (4) (1984) 333–350. doi:10.1016/0020-7683(84)90044-1.
[65] E. Sanchez-Palencia, Non-Homogeneous Media and Vibration Theory, Springer Berlin Heidelberg, 1980. doi:10.1007/3-540-10000-8.
[66] C. C. Mei, B. Vernescu, Homogenization Methods for Multiscale Mechanics, World Scientific, 2010. doi:10.1142/7427.
[67] R. S. Lakes, Foam structures with a negative Poisson's ratio, Science 235 (4792) (1987) 1038–1040. doi:10.1126/science.235.4792.1038.
[68] N. A. Fleck, V. S. Deshpande, M. F. Ashby, Micro-architectured materials: past, present and future, Proc. Math. Phys. Eng. Sci. 466 (2121) (2010) 2495–2516. doi:10.1098/rspa.2010.0215.
[69] P. Khaneh Masjedi, A. Maheri, P. M. Weaver, Large deflection of functionally graded porous beams based on a geometrically exact theory with a fully intrinsic formulation, Appl. Math. Modell. 76 (2019) 938–957. doi:10.1016/j.apm.2019.07.018.
[70] Z.-P. Wang, L. H. Poh, Y. Zhu, J. Dirrenberger, S. Forest, Systematic design of tetra-petals auxetic structures with stiffness constraint, Mater. Des. 170 (2019) 107669. doi:10.1016/j.matdes.2019.107669.
[71] G. W. Milton, A. V. Cherkaev, Which elasticity tensors are realizable?, J. Eng. Mater. Technol. 117 (4) (1995) 483–493. doi:10.1115/1.2804743.

Appendix A. Recall on Kirchhoff-Love plate theory

In a space endowed with an orthonormal reference $(O, \boldsymbol{e_1}, \boldsymbol{e_2}, \boldsymbol{e_3})$, let us consider a plane plate of thickness h normal to the axis $(O, \boldsymbol{e_3})$. For convenience, its mid-plane in the reference configuration is assumed to lie in the $(O, \boldsymbol{e_1}, \boldsymbol{e_2})$ plane.

Thin plate kinematics. The following kinematic assumptions are made: (1) all straight lines normal to the mid-surface remain straight and normal after deformation; (2) the thickness of the plate does not change during a deformation. This is the plate equivalent of the Euler-Bernoulli beam hypothesis. The displacement field $\boldsymbol{u}(x_1, x_2, x_3)$ of a thin planar plate is therefore defined as follows:

$$\begin{aligned} &\boldsymbol{u}(x_1, x_2, x_3) = \boldsymbol{v}(x_1, x_2) - x_3 \nabla v_3(x_1, x_2) \\ \Leftrightarrow &\begin{cases} u_1(x_1, x_2, x_3) = v_1(x_1, x_2) - x_3\, v_{3,x_1}(x_1, x_2) = v_1(x_1, x_2) - x_3\, r_3(x_1, x_2) \\ u_2(x_1, x_2, x_3) = v_2(x_1, x_2) - x_3\, v_{3,x_2}(x_1, x_2) = v_2(x_1, x_2) - x_3\, r_3(x_1, x_2) \\ u_3(x_1, x_2, x_3) = v_3(x_1, x_2) \end{cases} \end{aligned} \tag{A.1}$$

where $\boldsymbol{v}(x_1, x_2)$ is the displacement field of the mid-plane of the plate, and $\boldsymbol{r}(x_1, x_2) = \nabla v_3(x_1, x_2)$ are the rotations. Assuming the previous displacement field, the strain field $\boldsymbol{\varepsilon}$ reads:

$$\boldsymbol{\varepsilon} = \begin{bmatrix} \varepsilon_{11} & \varepsilon_{12} \\ \varepsilon_{12} & \varepsilon_{22} \end{bmatrix} = \begin{bmatrix} \dfrac{\partial v_1}{\partial x_1} & \dfrac{1}{2}\left(\dfrac{\partial v_1}{\partial x_2} + \dfrac{\partial v_2}{\partial x_1}\right) \\ \dfrac{1}{2}\left(\dfrac{\partial v_1}{\partial x_2} + \dfrac{\partial v_2}{\partial x_1}\right) & \dfrac{\partial v_2}{\partial x_2} \end{bmatrix} - x_3 \begin{bmatrix} \dfrac{\partial^2 v_3}{\partial x_1^2} & \dfrac{\partial^2 v_3}{\partial x_1 \partial x_2} \\ \dfrac{\partial^2 v_3}{\partial x_1 \partial y_1} & \dfrac{\partial^2 v_3}{\partial x_2^2} \end{bmatrix} = \boldsymbol{\mu} + z\boldsymbol{\chi} \tag{A.2}$$

where $\boldsymbol{\mu}$ represents the in-plane strains and $\boldsymbol{\chi}$ the out-of-plane curvatures. Units are: $[\boldsymbol{\mu}] = \mathrm{m.m^{-1}}$ and $[\boldsymbol{\chi}] = \mathrm{m^{-1}}$. Note that the out-of-plane strains ε_{i3} are all zero due to the chosen kinematic hypothesis. In particular, the normal out-of-plane strain ε_{33} is zero, which is generally not the case for thin structures, for which the plane stress behaviour is assumed.

Constitutive behaviour. The constitutive law of a thin plate has the following form:

$$\begin{bmatrix} \boldsymbol{N} \\ \boldsymbol{M} \end{bmatrix} = \begin{bmatrix} \boldsymbol{A} & \boldsymbol{B} \\ \boldsymbol{B} & \boldsymbol{D} \end{bmatrix} \begin{bmatrix} \boldsymbol{\mu} \\ \boldsymbol{\chi} \end{bmatrix} \tag{A.3}$$

where the tensor $\boldsymbol{A}$ describes the in-plane behaviour, the tensor $\boldsymbol{D}$ describes the bending behaviour, and their coupling is expressed through the tensor $\boldsymbol{B}$. The generalized stresses are the membrane stress $\boldsymbol{N}$ and bending moments $\boldsymbol{M}$, defined as follows:

$$\begin{cases} \boldsymbol{N} = \displaystyle\int_{-h^*/2}^{h^*/2} \boldsymbol{\sigma} dx_3 \\ \boldsymbol{M} = \displaystyle\int_{-h^*/2}^{h^*/2} x_3 \boldsymbol{\sigma} dx_3 \end{cases} \tag{A.4}$$

where $\boldsymbol{\sigma}$ denotes the stress field.

Appendix B. Two-scale analysis and effective coefficients

Since the panel thickness h is comparable to the unit cell size ℓ, we only need two-dimensional macroscopic coordinates $\boldsymbol{x} = (x_1, x_2)$ for in-plane variations:

$$x_1 = \epsilon y_1,\ x_2 = \epsilon y_2 \tag{B.1}$$

We assume that the material properties can be inhomogeneous but periodic on the microscale. Let the following two-scale asymptotic expansion for the displacement be introduced:

$$\boldsymbol{u}^\epsilon(\boldsymbol{x}) = \sum_{\alpha=0}^{+\infty} \epsilon^\alpha\, \boldsymbol{u}_\alpha\,(\boldsymbol{x}, \boldsymbol{y}), \quad \boldsymbol{y} = \frac{\boldsymbol{x}}{\epsilon}. \tag{B.2}$$

This leads to a series of problems for different orders of ϵ: at order ϵ^{-2}, we obtain that $u_0(x, y) = u_0(x)$. At order ϵ^{-1} we obtain the displacement field solutions of the unit cell problems. At order ϵ^0 we obtain the linear elastic constitutive equation averaged over the unit cell, yielding the following explicit energy formulation of the homogenised elastic plate tensor $\boldsymbol{A}^H$, $\boldsymbol{B}^H$ and $\boldsymbol{D}^H$ expressed in terms of their cartesian components as:

$$\begin{aligned}
A^H_{\alpha\beta\gamma\delta} =& \frac{1}{|Y|}\int_Y \boldsymbol{C}(\boldsymbol{y})\left(\boldsymbol{E}^{\alpha\beta} + \boldsymbol{\varepsilon}(\boldsymbol{w}^{\alpha\beta})\right) : \left(\boldsymbol{E}^{\gamma\delta} + \boldsymbol{\varepsilon}(\boldsymbol{w}^{\gamma\delta})\right) d\boldsymbol{y},\\
B^H_{\alpha\beta\gamma\delta} =& \frac{1}{|Y|}\int_Y \boldsymbol{C}(\boldsymbol{y})\left(\boldsymbol{E}^{\alpha\beta} + \boldsymbol{\varepsilon}(\boldsymbol{w}^{\alpha\beta})\right) : \left(y_3\boldsymbol{X}^{\gamma\delta} + \boldsymbol{\varepsilon}(\boldsymbol{\tau}^{\gamma\delta})\right) d\boldsymbol{y},\\
D^H_{\alpha\beta\gamma\delta} =& \frac{1}{|Y|}\int_Y \boldsymbol{C}(\boldsymbol{y})\left(y_3\boldsymbol{X}^{\alpha\beta} + \boldsymbol{\varepsilon}(\boldsymbol{\tau}^{\alpha\beta})\right) : \left(y_3\boldsymbol{X}^{\gamma\delta} + \boldsymbol{\varepsilon}(\boldsymbol{\tau}^{\gamma\delta})\right) d\boldsymbol{y},
\end{aligned} \tag{B.3}$$

where:

- $\boldsymbol{C}$ is the stiffness distribution at the scale of the unit cell.
- $\boldsymbol{E}^{\alpha\beta}$ designates a constant in-plane strain over the unit cell, resulting from the zero order displacement $\boldsymbol{u}_0$. There are three independent unit strain fields, namely the horizontal unit strain $\boldsymbol{E}^{11} = (1, 0, 0)^T$, the vertical strain $\boldsymbol{E}^{22} = (0, 1, 0)^T$ and the in-plane shear unit strain $\boldsymbol{E}^{12} = (0, 0, 1)^T$.
- $\boldsymbol{X}^{\alpha\beta}$ designates a constant flexural curvature over the unit cell, resulting from the zero order displacement $\boldsymbol{u}_0$. There are three independent unit strain fields, namely the horizontal unit flexure $\boldsymbol{X}^{11} = (1, 0, 0)^T$, the vertical unit flexure $\boldsymbol{X}^{22} = (0, 1, 0)^T$ and the shear unit flexure $\boldsymbol{X}^{12} = (0, 0, 1)^T$.
- $\boldsymbol{w}^{\alpha\beta}$ represents the displacement fields, solution of the following cell problem, expressed in its variational formulation here:

$$\begin{cases}
\text{Find admissible displacement } \boldsymbol{w}^{\alpha\beta} \text{ such that}\\
\displaystyle\int_Y \boldsymbol{C}(\boldsymbol{y})(\boldsymbol{E}^{\alpha\beta} + \boldsymbol{\varepsilon}(\boldsymbol{w}^{\alpha\beta})) : \boldsymbol{\varepsilon}(\boldsymbol{\phi})\, d\boldsymbol{y} = 0\\
\boldsymbol{w}^{\alpha\beta} \text{ is } (x_1, x_2)\text{-periodic.}
\end{cases} \tag{B.4}$$

  where $\boldsymbol{\phi}$ are admissible displacement vectors, i.e. with zero mean value and adequate smoothness. The generalized strain components $E^{\alpha\beta}$ are illustrated in Figure B.8(a-c).

- $\boldsymbol{\tau}^{\alpha\beta}$ represents the displacement fields, solution of to another cell problem governed by the following equations:

$$\begin{cases}
\text{Find admissible displacement } \boldsymbol{\tau}^{\alpha\beta} \text{ such that}\\
\displaystyle\int_Y \boldsymbol{C}(\boldsymbol{y})(y_3\boldsymbol{X}^{\alpha\beta} + \boldsymbol{\varepsilon}(\boldsymbol{\tau}^{\alpha\beta})) : \boldsymbol{\varepsilon}(\boldsymbol{\psi})\, d\boldsymbol{y} = 0\\
\boldsymbol{\tau}^{\alpha\beta} \text{ is } (x_1, x_2)\text{-periodic.}
\end{cases} \tag{B.5}$$

  where $\boldsymbol{\psi}$ are admissible displacement vectors, i.e. with zero mean value and adequate smoothness. The generalized strain components $y_3 X^{\alpha\beta}$ are illustrated in Figure B.8(d-f).

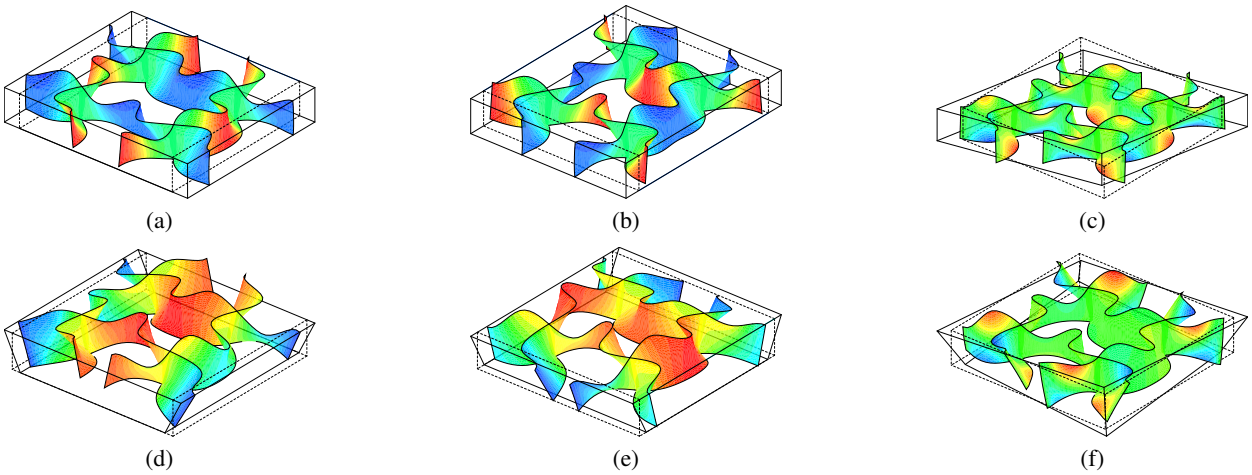

Figure B.8: Deformation modes of the six solutions of the cells problem (B.4) and (B.5), namely (a-b) two tractions, (c) in-plane shear, (d-e) two flexures, (f) shear flexure. The colors indicate the "normalized" value of the vertical displacement u_3 plotted on the deformed mesh. The deformed correspond to a tension up to 20% effective strain

In our study, the unit cell is described with shell elements. The numerical computation of the coefficients in (B.3) is solved numerically as follows:

$$
\begin{aligned}
A^H_{\alpha\beta\gamma\delta} &= \frac{1}{|Y|}\int_\omega \boldsymbol{C}(\boldsymbol{y})\left(\boldsymbol{E}^{\alpha\beta}+\left(\boldsymbol{\mu}(\boldsymbol{w}^{\alpha\beta})+y_3\boldsymbol{\chi}(\boldsymbol{w}^{\alpha\beta})\right)\right):\left(\boldsymbol{E}^{\gamma\delta}+\left(\boldsymbol{\mu}(\boldsymbol{w}^{\gamma\delta})+y_3\boldsymbol{\chi}(\boldsymbol{w}^{\alpha\beta})\right)\right)\,d\boldsymbol{y},\\
B^H_{\alpha\beta\gamma\delta} &= \frac{1}{|Y|}\int_\omega \boldsymbol{C}(\boldsymbol{y})\left(\boldsymbol{E}^{\alpha\beta}+\left(\boldsymbol{\mu}(\boldsymbol{w}^{\alpha\beta})+y_3\boldsymbol{\chi}(\boldsymbol{w}^{\alpha\beta})\right)\right):\left(y_3\boldsymbol{X}^{\gamma\delta}+\left(\boldsymbol{\mu}(\boldsymbol{\tau}^{\gamma\delta})+y_3\boldsymbol{\chi}(\boldsymbol{\tau}^{\alpha\beta})\right)\right)\,d\boldsymbol{y},\\
D^H_{\alpha\beta\gamma\delta} &= \frac{1}{|Y|}\int_\omega \boldsymbol{C}(\boldsymbol{y})\left(y_3\boldsymbol{X}^{\gamma\delta}+\left(\boldsymbol{\mu}(\boldsymbol{\tau}^{\gamma\delta})+y_3\boldsymbol{\chi}(\boldsymbol{\tau}^{\alpha\beta})\right)\right):\left(y_3\boldsymbol{X}^{\gamma\delta}+\left(\boldsymbol{\mu}(\boldsymbol{\tau}^{\gamma\delta})+y_3\boldsymbol{\chi}(\boldsymbol{\tau}^{\alpha\beta})\right)\right)\,d\boldsymbol{y},
\end{aligned}
\tag{B.6}
$$